Rapid Communications

Dual topological nodal line and nonsymmorphic Dirac semimetal in three dimensions

Yun-Tak Oh, Hong-Guk Min, and Youngkuk Kim*
Department of Physics, Sungkyunkwan University, Suwon 16419, Korea

(Received 3 January 2019; published 23 May 2019)

There are two types of previously known three-dimensional Dirac semimetals (DSs)—*topological* DSs and *nonsymmorphic* DSs. Here, we present a three-dimensional DS that exhibits features of both topological and nonsymmorphic DSs. We introduce a minimal tight-binding model for the space group 100 that describes a layered crystal made of two-dimensional planes in the *p*4*g* wallpaper group. Using this model, we demonstrate that double glide mirrors allow a noncentrosymmetric three-dimensional DS that hosts both symmetry-enforced Dirac points at time-reversal invariant momenta and twofold-degenerate Weyl nodal lines on a glide-mirror-invariant plane in momentum space. The proposed DS allows for rich topological physics manifested in both topological surface states and topological phase diagrams, which we discuss in detail. We also perform first-principles calculations to predict that the proposed DS is realized in a set of existing materials BaLaXBY_5, where X = Cu or Au, and Y = O, S, or Se.

DOI: 10.1103/PhysRevB.99.201110

Dirac semimetals (DSs) refer to a class of topological semimetals, characterized by hosting massless Dirac fermions in momentum space [1]. First identified in graphene with vanishingly weak spin-orbit coupling (SOC), there has been a surge of interest in massless Dirac fermion systems, exhibiting exotic properties and potential applications for future electronic devices [2,3]. Notably, with the advent of topological insulators [4,5], three-dimensional (3D) DSs with strong spin-orbit coupling have reinforced their status as an important class of topological semimetals. It was first noted that a 3D DS can occur at the phase boundary between the topological and the normal insulators in the presence of inversion symmetry [6,7]. Later, Young *et al.* found that the 3D DSs can be stabilized by crystalline symmetries and time-reversal symmetry [8], and Wang *et al.* theoretically proposed material realizations in Na_3Bi and Cd_3As_2 [9,10], which were confirmed experimentally [11–15]. Currently, the DSs are expected to exist in a variety of forms, such as two-dimensional (2D) DSs [16], double DSs [17], type-II DSs [18], and Dirac-Weyl semimetals [19].

In spite of this variety, it is surprising to notice that all the previously known DSs fall into two disjoint classes, dubbed *topological* and *nonsymmorphic* DSs, respectively [20]. The nonsymmorphic class of DSs is characterized by hosting Dirac points (DPs) that are pinned at the time-reversal invariant momenta (TRIM) of the Brillouin zone (BZ). On the other hand, the topological class of DSs distinguishes itself from nonsymmorphic DSs by having a pair of DPs off TRIM. Another distinguishing feature of topological DSs is the coexistence of nontrivial band topology in the bulk, manifested as gapless excitations on the surface [21,22]. In contrast, the bulk bands of nonsymmorphic DSs are expected to be topologically trivial. Instead, the topological nature of the nonsymmorphic class is reflected in topological phase transitions, driven by symmetry-lowering perturbations from the nonsymmorphic DS into either a topological insulator or a normal insulator [8,20,23–25].

In this Rapid Communication we provide an exception to this *a priori* classification of 3D DSs. Developing a minimal tight-binding model for space groups (SGs) *P*4*bm* (No. 100), we establish the existence of another type of 3D DS, characterized by featuring both *topological nodal lines* and *nonsymmorphic* DSs. It is shown that the DS hosts the DPs that reside at TRIM, which is a characteristic feature of nonsymmorphic DSs. Simultaneously, the bulk bands carry nontrivial band topology, giving rise to topological surface states, which is unexpected from the previously known nonsymmorphic Dirac semimetals. A striking consequence of this dual nonsymmorphic and topological nature of the DS is the rich topological physics manifested not only in the surface energy spectrum but also in topological phase transitions driven by symmetry-breaking perturbations. Drumheadlike topological surface states arise due to the nontrivial band topology in the bulk, characterized by hosting Weyl nodal lines (WNLs). Moreover, symmetry-lowering perturbations derive a topological phase transition from the proposed DS to distinct topological phases, including a weak topological insulator (WTI) and Weyl and double Weyl semimetal (WS) phases. Using first-principles calculations, we also discuss its material realization in an existing compound, $BaLaCuBO_5$.

Let us begin by elucidating the role of symmetries in SG 100 to protect the degeneracies of the Bloch states. SG 100 has the distinguishing feature that it is generated by a glide mirror g_x and a fourfold rotation C_{4z} without inversion symmetry. As emphasized in Refs. [26,27], the double glide mirrors, g_x and $g_y = C_{4z}^{-1} g_x C_{4z}$, together with time-reversal symmetry $\mathcal{T}$, span four-dimensional irreducible representations (FDIRs) at $M = (\pi, \pi, 0)$ and $A = (\pi, \pi, \pi)$, where g_x and g_y satisfy the minimal algebras for a FDIR, $g_x^2 = g_y^2 = 1$ and $[\mathcal{T}, g_{x(y)}] = \{g_x, g_y\} = 0$. Moreover, the linear dispersion of the bands

*youngkuk@skku.edu

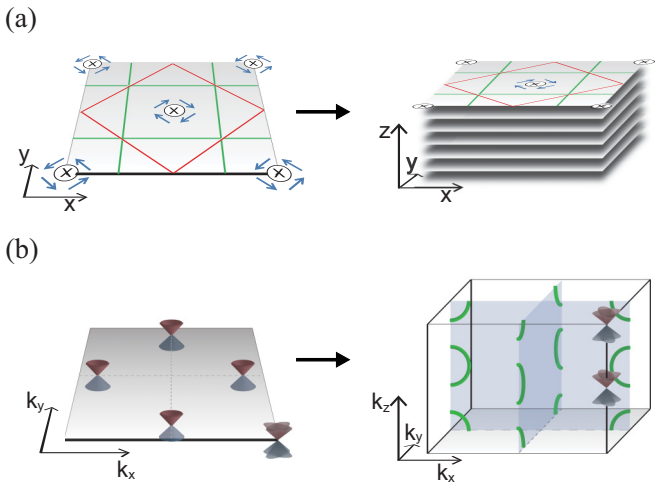

FIG. 1. (a) Schematic illustration of a two-dimensional (2D) layer in the $p4g$ wallpaper group (left panel) and an infinite stack of the $p4g$ layers (right panel). The red (green) lines represent mirror (glide-mirror-) invariant lines. The center of the C_{4z} rotational axis is designated by the $\otimes$ symbol. (b) Corresponding BZ in two (left) and three (right) dimensions. The locations of the twofold-degenerate WPs and fourfold-degenerate DPs are indicated by the Weyl and the double Weyl (Dirac) cones, respectively. The location of WNLs in the 3D BZ is indicated by green lines.

is generic at M and A since a $\mathcal{T}$-odd vector representation of the point group at the M and A points is present in the tensor product of the FDIRs [8,17,26]. Therefore, the presence of DPs is enforced in SG 100 when the filling is an odd multiple of four. In addition, g_x (g_y) and $\mathcal{T}$ further give rise to a constraint to the connectivity of the bands, such that the Kramers pairs at Γ and $Y(X)$ should exchange their partners from Γ to $Y(X)$ without opening a band gap, leading to an hourglasslike connectivity [27–29]. As a consequence, it is guaranteed that additional twofold-degenerate WNLs are present on the $k_x = 0$ ($k_y = 0$) plane, protected by glide mirror g_x (g_y).

The above symmetry analysis provides a guiding principle to design the DS hosted in SG 100. Since SG 100 and the $p4g$ wallpaper group are equivalent, generated by C_{4z} and g_x, a minimal four-band tight-binding model can be constructed from an infinite stack of the identical layer in the $p4g$ wallpaper group as illustrated in Fig. 1. The constructed lattice model is presented in Fig. 2(a). A unit cell comprises two sublattices A and B (labeled by $\tau_z = \pm 1$), which are coordinated at $\boldsymbol{d}(\tau_z) = \frac{1}{4}[(2+\tau_z)\boldsymbol{a}_x + (2-\tau_z)\boldsymbol{a}_y]$, respectively. The corresponding tight-binding Hamiltonian is given as

$$\mathcal{H}^0(\boldsymbol{k}) = \mathcal{H}^t(\boldsymbol{k}) + V(\boldsymbol{k}), \tag{1}$$

where

$$\mathcal{H}^t(\boldsymbol{k}) = t_1 \cos\frac{k_x}{2}\cos\frac{k_y}{2}\tau_x + t_2(\cos k_x + \cos k_y) + t_3 \cos k_z$$

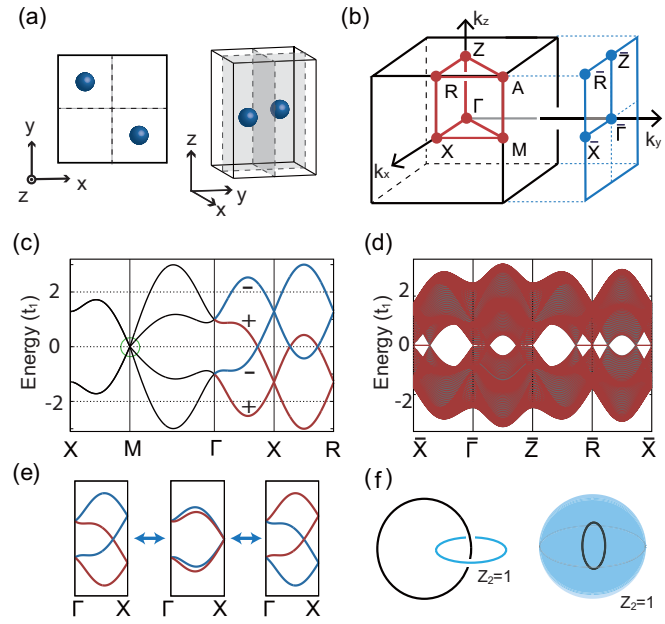

FIG. 2. (a) Model lattice for SG 100. The glide planes are represented by dashed boxes. (b) Bulk tetragonal and surface rectangular BZs. (c) Electronic energy bands for SG 100, calculated from (1) with the parameter set $\{t_1, t_2, t_3, v_0, v_1, v_2, v_3, v_4\} = \{0.35, 0, 0, 0, 0.5, 0.6, 0.45\}$. The bands in the + and − eigensectors of g_y (g_x) are colored red and blue, respectively. The DP is indicated by a dashed (green) circle. (d) Bulk (gray) and slab (red) energy bands. Topological surface states emerge in the interior region of the projected nodal lines, where $\overline{X}$ and $\overline{R}$ are contained. (e) Schematic illustration of band inversion at X (R). (f) Topological characterization of twofold-degenerate nodal lines in SG 100.

describes the nearest hopping of electrons, and

$$V(\boldsymbol{k}) = v_0 \cos\frac{k_x}{2}\cos\frac{k_y}{2}\tau_y\sigma_z + v_1(\sin k_x\,\sigma_x + \sin k_y\,\sigma_y)\tau_z + v_2(\sin k_x\,\sigma_y - \sin k_y\,\sigma_x) + v_3 \sin k_z\tau_z\sigma_z + v_4\left(\sin\frac{k_x}{2}\cos\frac{k_y}{2}\sigma_y - \cos\frac{k_x}{2}\sin\frac{k_y}{2}\sigma_x\right)\tau_x$$

describes the potential terms that lower the transnational symmetry of $\mathcal{H}^t(\boldsymbol{k})$ into SG 100. $V(\boldsymbol{k})$ is constructed, such that it preserves the generators of SG 100, $g_x = \tau_x \exp(-i\frac{\pi}{2}\sigma_x)$ and $C_{4z} = \exp(-i\frac{\pi}{4}\sigma_z)$, and time-reversal symmetry $\mathcal{T} = i\sigma_y K$, where $\{\sigma_i\}_{i=x,y,z}$ are the Pauli matrices for spins. We adopted a gauge in which the Hamiltonian $\mathcal{H}^0(\boldsymbol{k})$ transforms under the translation of a reciprocal lattice vector $\boldsymbol{G}$ according to

$$\mathcal{H}^0(\boldsymbol{k}+\boldsymbol{G}) = e^{-i\boldsymbol{d}(\tau_z)\cdot\boldsymbol{G}}\mathcal{H}^0(\boldsymbol{k})e^{i\boldsymbol{G}\cdot\boldsymbol{d}(\tau_z)}.$$

Figure 2(c) shows the electronic energy bands calculated from the tight-binding model Eq. (1). Without the inversion symmetry, each band along the high-symmetry M-Γ-X-R line is nondegenerate, thus forming a fourfold degeneracy at M. Note that the bands are linearly dispersing in the vicinity of M point. Therefore, the bands feature a nonsymmorphic DP at M. We also have confirmed that an additional DP is present at A, as we expected from the symmetry analysis. Based on

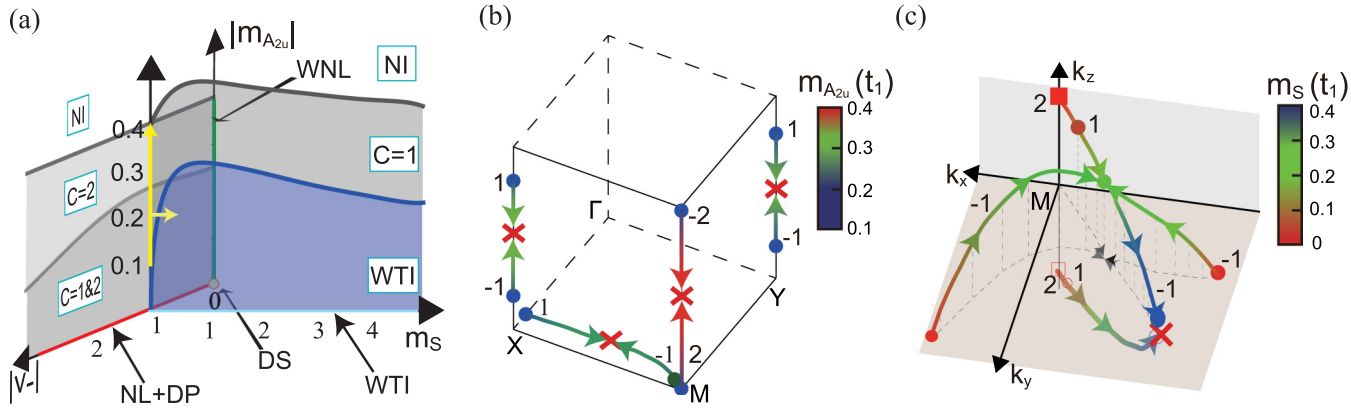

FIG. 3. Topological phase diagram and topological phase transitions induced by symmetry-lowering perturbations from the DS in SG 100. (a) Topological phase diagram in the $(v_-, m_s, m_{A_{2u}})$-parameter space in the unit of t_1. The DS in SG 100 resides along the $|v_-|$ axis (colored red), which is connected with a centrosymmetric DS at the origin, where $(v_-, m_s, m_{A_{2u}}) = (0, 0, 0)$ (indicated by a yellow circle). A WNL semimetal appears along the $|m_{A_{2u}}|$ axis (green line). The WS phases are present in the gray-colored regions on the $m_s - |m_{A_{2u}}|$ and $|v_-| - |m_{A_{2u}}|$ planes. The WS phase carrying both double ($|\mathcal{C}| = 2$) and single ($|\mathcal{C}| = 1$) WPs is distinguished from the WS phase carrying only double ($|\mathcal{C}| = 2$) WPs with a thicker gray color on the $|v_-| - |m_{A_{2u}}|$ plane. A WTI phase is colored blue on the $m_s - |m_{A_{2u}}|$ plane. The remaining white area represents the trivial insulator phase. (b) Evolution of the WPs as a function of $m_{A_{2u}}$ during the topological phase transition occurring along the vertical yellow line in (a). The numbers near a trajectory indicate the corresponding Chern number of the WPs. A color scheme is used to indicate the magnitude of $m_{A_{2u}}$ at $m_s = 0$ and $v_- = 1.0$. The WPs are annihilated at the red crosses. (c) Evolution of the WPs as a function of m_s during the topological phase transition occurring along the horizontal yellow line in (a). A square (circle) represents a $|\mathcal{C}| = 2$ ($|\mathcal{C}| = 1$) WP.

the Wilson band calculations [30], we find that the DPs carry the zero Chern number [31]. This indicates that the fourfold degeneracy is a genuine DP, in the sense that it is a composite of two WPs with ± 1 Chern numbers, respectively.

Besides the fourfold degeneracy, we find that the bands also feature twofold-degenerate WNLs, the hourglasslike band connectivity on the high-symmetry Γ-X (Z-R) line. This guarantees the presence of a twofold degeneracy on the $k_y = 0$ plane, as shown in Fig. 2(c). A close inspection of the entire BZ reveals that one-dimensional nodal lines are present in the vicinity of X (R) lying on the $k_y = 0$ plane. We have confirmed that a Weyl line node carries the π Berry phase, calculated along a $C_2\mathcal{T}$-invariant path that threads the nodal line [see the left panel of Fig. 2(f)], where the Berry phase is $\mathbb{Z}_2$ quantized. As a consequence of the π Berry phase, drumheadlike states emerge on the surface where the projected interior region of a nodal line has nonzero area, such as the (100) surface. As shown in Fig. 2(d), the slab band calculation results in the topological surface states at $E = 0$ near the $\overline{\Gamma}$ ($\overline{R}$), which constitute a part of the drumheadlike surface states on the (010) surface.

The WNL hosted in SG 100 is of an hourglass type [32–34], which is robust against the band inversion at M (R). As illustrated in Fig. 2(e), the band inversion at X shrinks the size of the nodal line into a fourfold-degenerate DP. However, instead of annihilating it, the band inversion reverts the DP to a nodal line due to the hourglasslike band connectivity. We assert that this type of WNL can be characterized by a nontrivial $\mathcal{Z}_2$ topological invariant, calculated on the time-reversal invariant sphere that encloses a nodal line [see the right panel of Fig. 2(f)]. The Wilson band calculation results in the same connectivity of the Wilson bands as those of a 3D Dirac point [31]. The nontrivial $\mathcal{Z}_2$ invariant, again, reveals that the WNL can be shrunk to form a 3D DP.

Having demonstrated the *topological* aspect of the DS, we now move to its *nonsymmorphic* aspect, captured in a topological phase diagram shown in Fig. 3. From the DS phase, we consider symmetry-lowering perturbations [31]. Among diverse possibilities, as a representative example, here we consider a combination of the inversion symmetric E_g- and B_{2g}-mode strains and an $m_{A_{2u}}$-mode staggered potential. These perturbations are described by a perturbed Hamiltonian $\mathcal{H}^1(\boldsymbol{k})$, where

$$\mathcal{H}^1(\boldsymbol{k}) = m_{E_g} \sin\left(\frac{k_x + k_y}{2}\right)\tau_y + m_{B_{2g}} \sin\frac{k_x}{2} \sin\frac{k_y}{2}\tau_x + m_{A_{2u}}\tau_z. \tag{2}$$

For simplicity, we assume the mass parameters are equivalent between the inversion-symmetric perturbations ($m_s \equiv m_{E_g} = m_{B_{2g}}$). Furthermore, we decompose the pristine Hamiltonian $\mathcal{H}^0(\boldsymbol{k})$ [Eq. (1)] into the inversion-symmetric part $\mathcal{H}^0_+(\boldsymbol{k})$ and inversion-asymmetric part $\mathcal{H}^0_-(\boldsymbol{k})$, where

$$\mathcal{H}^0_+ = t_1 \cos\frac{k_x}{2}\cos\frac{k_y}{2}\tau_x + v_1(\sin k_x\tau_z\sigma_x + \sin k_y\tau_z\sigma_y) + v_3 \sin k_z\tau_z\sigma_z, \tag{3}$$

and

$$\mathcal{H}^0_- = v_-\left[v_0 \cos\frac{k_x}{2}\cos\frac{k_y}{2}\tau_y\sigma_z + v_2(\sin k_x\,\sigma_y - \sin k_y\,\sigma_x) + v_4\left(\sin\frac{k_x}{2}\cos\frac{k_y}{2}\sigma_y - \cos\frac{k_x}{2}\sin\frac{k_y}{2}\sigma_x\right)\tau_x\right]. \tag{4}$$

Here, v_- is introduced to parametrize the overall strength of the inversion-asymmetric part.

Figure 3(a) shows a topological phase diagram that is obtained from $\mathcal{H}^0 + \mathcal{H}^1$ in the $(v_-, m_s, m_{A_{2u}})$ space. We first

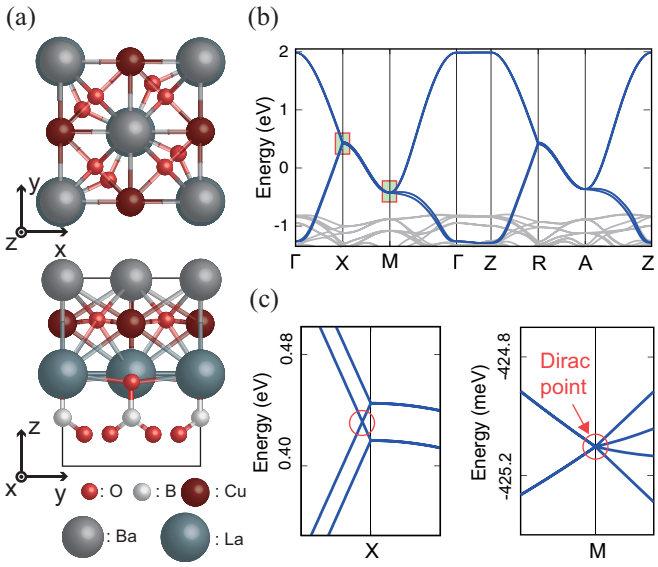

FIG. 4. Atomic and electronic structures of $BaLaCuBO_5$. (a) Top view (top panel) and side view (bottom panel) of the atomic structure. (b) Electronic energy band structure. The unit cell is indicated by a solid box. The DFT (Wannier) energy bands are colored gray (blue). The Wannierzation exactly reproduces the four DFT bands near the Fermi level. (c) Magnified views of the red rectangles in (b) at X (left panel) and at M (right panel). The WNL and DP are indicated by a red circle.

note that the DS phase in SG 100 resides along the $|v_-|$ (red) axis. From this DS phase, a centrosymmetric strain, described by m_s, drives a topological phase transition; positive (negative) m_s induces a WTI (normal insulator), characterized by $\mathbb{Z}_2$ topological indices $(\mu_0;\mu_1,\mu_2,\mu_3) = (0;001)$ $[(0;000)]$. Therefore, the DS phase defines a phase boundary between the normal and topological insulator phases [7], thus exhibiting the nonsymmorphic nature of the DS. In addition to the WTI phase, we find that a Weyl semimetal (WS) can also be induced from the DS phase by applying the staggered potential ($|m_{A_{2u}}| > 0$). Interestingly, we find that three distinctive WS phases are allowed: (1) one having regular (single) WPs with the Chern number $|\mathcal{C}| = 1$, (2) another having double WPs with $|\mathcal{C}| = 2$, and (3) the other having both single and double WPs. We also note that an archetypal centrosymmetric DS phase is restored from the DS phase by turning off the noncentrosymmetric interactions $v_- = 0$, from which a WNL semimetal phase is induced by the m_s strains, represented by a vertical green line in the figure.

Figure 3(b) illustrates the detailed process of topological phase transition via the creation and annihilation of WPs along the vertical (yellow) path indicated in Fig. 3(a). When varying $m_{A_{2u}}$ from 0.1 to 0.4 in the unit of t_1, the in-plane $\mathcal{C} = 1$ WP near X (Y) and the in-plane $\mathcal{C} = -1$ WP near the DP of M fuse and annihilate eventually, while the WPs residing on the k_z axis find their antichiral partners by moving along the k_z axis. This inter-TRIM WP annihilation results in the trivial insulator phase. On the other hand, Fig. 3(c) illustrates the evolution of the WPs during the topological phase transition from the WS with $\mathcal{C} = 2$ to the WTI phase that occurs along the horizontal (yellow) path indicated in Fig. 3(a). Apart from zero, $m_s > 0$ splits a WP with $\mathcal{C} = 2$ into two $\mathcal{C} = 1$ WPs off the k_z axis. One of the two $\mathcal{C} = 1$ WPs encounters the other two $\mathcal{C} = -1$ WPs from the $k_z = 0$ plane. This event results in a single $\mathcal{C} = -1$ WP, indicated by a solid green circle. The resultant $\mathcal{C} = -1$ WP is eventually annihilated on the $k_z = 0$ plane by meeting with another WP with $\mathcal{C} = 1$, which originates from the double WP on the k_z axis. This annihilation results in a WTI [31].

Finally, searching for materials that realize the DS in SG 100, we have found an existing material, $BaLaCuBO_5$ [35]. $BaLaCuBO_5$ is a layered system in SG 100 as shown in Fig. 4(a). It comprises $p4g$ multilayers with each layer preserving C_{4z} rotation and double glide-mirror g_x and g_y symmetries. Our first-principles calculations, performed using the QUANTUM ESPRESSO package [36], support that $BaLaCuBO_5$ realizes the proposed DS phase [31]. Figures 4(b) and 4(c) show the first-principles electronic energy bands of $BaLaCuBO_5$. The sticking of four bands is clear from the band structure, featuring filling-enforced gaplessness [37]. A fourfold-degenerate DP is present at M, and the hourglasslike band connectivity appears on the Γ-X line. The hourglasslike band connectivity leads to a band crossing on the Γ-X line, as shown in the magnified view in Fig. 4(d). The presence of band crossing signals the presence of a WNL that encircles the M point lying on the $k_x = 0$ plane, which we have confirmed throughout the band calculations performed in the entire BZ. Our results are in good agreement with the online time-reversal invariant topological encyclopedia, which indicates $BaLaCuBO_5$ is a high-symmetry point topological semimetal [38].

In conclusion, we have established the existence of another type of DS in three dimensions, characterized by hosting topological surface states and mediating topological phase transitions. Hosting topological surface states in nonsymmorphic DSs, the proposed DS features a unique topological character unlike archetypal 3D DSs. The surface energy spectrum should give rise to drumheadlike topological surface states, which should be feasible to observe in the $BaLaCuBO_5$ compound using a known experimental technique, such as angle-resolved photoemission spectroscopy (ARPES). Moreover, defining a symmetry-tuned topological critical point between a normal insulator and a WTI, the proposed DS can transform to diverse topological phases by symmetry-lowering perturbations.

This work was supported by the National Research Foundation of Korea (NRF) grant funded by the government of Korea (MSIP; Ministry of Science, ICT & Future Planning) (No. NRF-2017R1C1B5018169). The computational resource was provided from the Korea Institute of Science and Technology Information (KISTI).

[1] N. P. Armitage, E. J. Mele, and A. Vishwanath, Rev. Mod. Phys. **90**, 015001 (2018).
[2] A. K. Geim, Science **324**, 1530 (2009).
[3] M. J. Allen, V. C. Tung, and R. B. Kaner, Chem. Rev. **110**, 132 (2010).
[4] M. Z. Hasan and C. L. Kane, Rev. Mod. Phys. **82**, 3045 (2010).

[5] X.-L. Qi and S.-C. Zhang, Rev. Mod. Phys. **83**, 1057 (2011).

[6] L. Fu, C. L. Kane, and E. J. Mele, Phys. Rev. Lett. **98**, 106803 (2007).

[7] S. Murakami, New J. Phys. **10**, 029802 (2008).

[8] S. M. Young, S. Zaheer, J. C. Y. Teo, C. L. Kane, E. J. Mele, and A. M. Rappe, Phys. Rev. Lett. **108**, 140405 (2012).

[9] Z. Wang, Y. Sun, X.-Q. Chen, C. Franchini, G. Xu, H. Weng, X. Dai, and Z. Fang, Phys. Rev. B **85**, 195320 (2012).

[10] Z. Wang, H. Weng, Q. Wu, X. Dai, and Z. Fang, Phys. Rev. B **88**, 125427 (2013).

[11] Z. K. Liu, B. Zhou, Y. Zhang, Z. J. Wang, H. M. Weng, D. Prabhakaran, S.-K. Mo, Z. X. Shen, Z. Fang, X. Dai, Z. Hussain, and Y. L. Chen, Science **343**, 864 (2014).

[12] S.-Y. Xu, C. Liu, S. Kushwaha, T.-R. Chang, J. Krizan, R. Sankar, C. Polley, J. Adell, T. Balasubramanian, K. Miyamoto *et al.*, arXiv:1312.7624.

[13] S. Borisenko, Q. Gibson, D. Evtushinsky, V. Zabolotnyy, B. Büchner, and R. J. Cava, Phys. Rev. Lett. **113**, 027603 (2014).

[14] M. Neupane, S.-Y. Xu, R. Sankar, N. Alidoust, G. Bian, C. Liu, I. Belopolski, T.-R. Chang, H.-T. Jeng, H. Lin, A. Bansil, F. Chou, and M. Z. Hasan, Nat. Commun. **5**, 3786 (2014).

[15] Z. K. Liu, J. Jiang, B. Zhou, Z. J. Wang, Y. Zhang, H. M. Weng, D. Prabhakaran, S.-K. Mo, H. Peng, P. Dudin, T. Kim, M. Hoesch, Z. Fang, X. Dai, Z. X. Shen, D. L. Feng, Z. Hussain, and Y. L. Chen, Nat. Mater. **13**, 677 (2014).

[16] B. J. Wieder and C. L. Kane, Phys. Rev. B **94**, 155108 (2016).

[17] B. J. Wieder, Y. Kim, A. M. Rappe, and C. L. Kane, Phys. Rev. Lett. **116**, 186402 (2016).

[18] T.-R. Chang, S.-Y. Xu, D. S. Sanchez, W.-F. Tsai, S.-M. Huang, G. Chang, C.-H. Hsu, G. Bian, I. Belopolski, Z.-M. Yu, S. A. Yang, T. Neupert, H.-T. Jeng, H. Lin, and M. Z. Hasan, Phys. Rev. Lett. **119**, 026404 (2017).

[19] H. Gao, Y. Kim, J. W. F. Venderbos, C. L. Kane, E. J. Mele, A. M. Rappe, and W. Ren, Phys. Rev. Lett. **121**, 106404 (2018).

[20] B.-J. Yang and N. Nagaosa, Nat. Commun. **5**, 4898 (2014).

[21] M. Kargarian, M. Randeria, and Y.-M. Lu, Proc. Natl. Acad. Sci. USA **113**, 8648 (2016).

[22] G. Bednik, Phys. Rev. B **98**, 045140 (2018).

[23] J. A. Steinberg, S. M. Young, S. Zaheer, C. L. Kane, E. J. Mele, and A. M. Rappe, Phys. Rev. Lett. **112**, 036403 (2014).

[24] L. M. Schoop, M. N. Ali, C. Straßer, A. Topp, A. Varykhalov, D. Marchenko, V. Duppel, S. S. P. Parkin, B. V. Lotsch, and C. R. Ast, Nat. Commun. **7**, 11696 (2016).

[25] B.-J. Yang, T. A. Bojesen, T. Morimoto, and A. Furusaki, Phys. Rev. B **95**, 075135 (2017).

[26] S. Zaheer, Three dimensional Dirac semimetals, Ph.D. thesis, University of Pennsylvania, 2014.

[27] B. J. Wieder, B. Bradlyn, Z. Wang, J. Cano, Y. Kim, H.-S. D. Kim, A. M. Rappe, C. L. Kane, and B. A. Bernevig, Science **361**, 246 (2018).

[28] S. M. Young and C. L. Kane, Phys. Rev. Lett. **115**, 126803 (2015).

[29] Z. Wang, A. Alexandradinata, R. J. Cava, and B. A. Bernevig, Nature (London) **532**, 189 (2016).

[30] R. Yu, X. L. Qi, A. Bernevig, Z. Fang, and X. Dai, Phys. Rev. B **84**, 075119 (2011).

[31] See Supplemental Material at http://link.aps.org/supplemental/10.1103/PhysRevB.99.201110 for details of the Wilson band calculations, detailed results of the topological invariants, the classification of the perturbations by the point group D_{4h}, detailed calculations of the associated topological invariants, and details of computational methods and the first-principles results for other candidates.

[32] T. Bzdušek, Q. Wu, A. Rüegg, M. Sigrist, and A. A. Soluyanov, Nature (London) **538**, 75 (2016).

[33] L. Wang, S.-K. Jian, and H. Yao, Phys. Rev. B **96**, 075110 (2017).

[34] S.-S. Wang, Y. Liu, Z.-M. Yu, X.-L. Sheng, and S. A. Yang, Nat. Commun. **8**, 1844 (2017).

[35] R. Norrestam, M. Kritikos, and A. Sjoedin, Acta Crystallogr., Sect. B: Struct. Sci. **50**, 631 (1994).

[36] P. Giannozzi, S. Baroni, N. Bonini, M. Calandra, R. Car, C. Cavazzoni, D. Ceresoli, G. L. Chiarotti, M. Cococcioni, I. Dabo, A. D. Corso, S. de Gironcoli, S. Fabris, G. Fratesi, R. Gebauer, U. Gerstmann, C. Gougoussis, A. Kokalj, M. Lazzeri, L. Martin-Samos *et al.*, J. Phys.: Condens. Matter **21**, 395502 (2009).

[37] H. Watanabe, H. C. Po, M. P. Zaletel, and A. Vishwanath, Phys. Rev. Lett. **117**, 096404 (2016).

[38] T. Zhang, Y. Jiang, Z. Song, H. Huang, Y. He, Z. Fang, H. Weng, and C. Fang, Nature (London) **566**, 475 (2019).